Nano Research

Open Access

Research Article

Open-hollow porous carbon-supported NiCo dual single atom catalyst with hydrophilic surface for enhanced oxygen reduction and hydrogen evolution reaction

Xinxin Liang[1,§] ✉, Yihan Wang[1,§], Fengshou Tian[1], Panlong Liu[1], Zeyu Fan[3], Guoqing Wang[1], Hirofumi Yoshikawa[4], Heng Wang[2] ✉, and Jianbo Zhao[1] ✉

[1] *College of Material and Chemical Engineering, Key Laboratory of Surface and Interface Science and Technology of Henan Province, Zhengzhou University of Light Industry, Zhengzhou 450002, China*
[2] *College of New Energy, Collaborative Innovation Center for New Energy Vehicle of Henan Province, Henan International Joint Laboratory of Ceramic Energy Materials, Zhengzhou University of Light Industry, Zhengzhou 450002, China*
[3] *Changjiang River Scientific Research Institute, Research Center of Water Engineering Safety and Disaster Prevention of Ministry of Water Resources, Wuhan 430010, China*
[4] *Kwansei Gakuin University, 1 Gakuen Uegahara, Sanda, Hyogo 669-1330, Japan*
[§] *Xinxin Liang and Yihan Wang contributed equally to this work.*

Cite this article: *Nano Research*, **2026**, *19*, 94908401. https://doi.org/10.26599/NR.2026.94908401

ABSTRACT: The pursuit of high-performance, platinum-free electrocatalysts for the oxygen reduction reaction (ORR) and hydrogen evolution reaction (HER) is fundamentally limited by the challenges of inadequate intrinsic activity and poor accessibility of active sites in single atom catalysts. Herein, the bimetallic single-atom NiCo/nitrogen-doped carbon (NC)-tannic acid (TA) electrocatalyst with the unclosed hollow morphology was constructed by the modification of precursor. Within this structure, hierarchical porous architecture, and surface hydrophilicity synergistically enhance the exposure and accessibility of active sites. Theoretical calculations confirm that the introduction of Ni facilitates electron transfer from Co sites, resulting in a downshifted d-band center. This electronic configuration effectively mitigates the over-adsorption of reaction intermediates, thereby reducing the energy barriers for both reactions. In alkaline ORR test, NiCo/NC-TA outperformed Pt/C-20% in both activity and stability, achieving a half-wave potential of 0.896 V and retaining 98% of the current after 10 h durability testing. Moreover, NiCo/NC-TA-based Zn–air batteries delivered a high open-circuit voltage of 1.49 V, a specific capacity of 764.1 mAh·g^{-1}, and long-term cycling stability. Notably, the catalyst also exhibited enhanced HER activity, with a low overpotential of 92 mV in alkaline media, matching Pt/C-20% performance at a current density of 120 mA·cm^{-2}. This work provides an approach for designing electrocatalysts through the integration of porosity engineering and electronic synergy, which could be extended to other energy-related material systems.

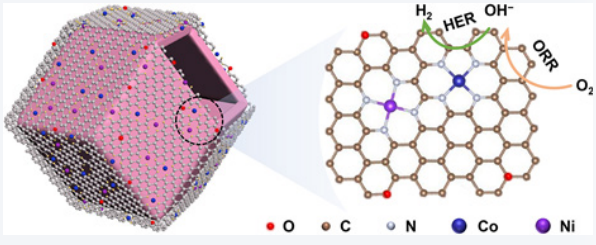

KEYWORDS: dual single atom catalyst, hydrophilicity, oxygen reduction reaction, hydrogen evolution reaction

1 Introduction

The shift toward sustainable energy systems has spurred research into fuel cells, metal–air batteries, and water electrolysis [1, 2]. The hydrogen evolution reaction (HER) is pivotal for sustainable fuel production, while the oxygen reduction reaction (ORR) is indispensable for its application in electrochemical power generation. While these two complementary processes constitute a fundamental carbon-neutral energy loop, the efficacy of these core reactions is hindered by intrinsic kinetic barriers [3]. Platinum (Pt)-based catalysts exhibit benchmark performance, but their scarcity has motivated the research for non-precious alternatives [4, 5]. Catalysts based on transition metals, such as Fe, Co, and Ni, have been proven to be highly promising electrocatalytic materials for ORR and HER [6–8]. Among them, single atom catalysts (SACs), particularly Co–N–C structures, have emerged as promising candidates due to the high atomic utilization, and superior stability

Received: November 29, 2025; **Revised:** December 31, 2025
Accepted: January 2, 2026

✉Address correspondence to Xinxin Liang, 2023014@zzuli.edu.cn; Heng Wang, wangheng@zzuli.edu.cn; Jianbo Zhao, zhaojianbo@zzuli.edu.cn

compared to Fe-based counterparts, which suffer from Fenton reactions [9, 10]. As reported, theoretical studies comparing NiN_4-C, FeN_4-C, and CoN_4-C catalysts reveal the potential of CoN_4-C as a bifunctional catalyst for ORR and HER [11]. However, the performance of Co–N–C SACs remains suboptimal, primarily stemming from the limited intrinsic activity of Co–N_4 sites, as well as the insufficient accessibility of active sites that are often buried within microporous carbon matrices derived from conventional synthesis [12].

Electronic structure engineering induces electronic coupling effect at adjacent heterometallic sites and synergistically modulates the adsorption energy of intermediates, circumventing the linear constraint from Sabatier principle [13, 14]. Given the electronegativity trend (Fe < Co < Ni), Ni introduction would reduce electron density at the active site, preventing the strong adsorption and achieving optimal intermediate binding, thus enhancing oxygen electrocatalysis [15]. Indeed, previous studies have reported on the bifunctional and bifunctional properties of Ni, Co-based materials, particularly their dual catalytic activity in ORR and HER [16–19]. The Kundu team synthesized a multi-layered N-doped graphitic carbon nanotube (CNT) coated NiCo alloy, which exhibited trifunctional electrocatalytic activity for ORR, oxygen evolution reaction (OER), and HER [16]. Pan and others prepared a NiCo single-atom electrocatalyst via pyrolysis method, which exhibits excellent ORR and HER bifunctional activity [19]. On the other hand, architectural engineering is critical to ensure active site accessibility in overall electrocatalytic performance [20]. Poor active site accessibility in SACs derived from conventional metal–organic frameworks (MOF)-pyrolysis stems from restricted proton/gas transport in micropore structure and the inherent low wettability of the carbon matrix [15, 21]. The wettability of carbon materials is synergistically governed by surface chemistry, topographical architecture, and inherent properties [22, 23]. Primary strategies for improving catalyst hydrophilicity include surface chemical modification and pore structure optimization, such as surface oxidation, polar group modification, porous structure design, or plasma treatment [23, 24].

Herein, we report a unified etching-pyrolysis strategy to construct an unclosed hollow bimetallic single atom catalyst (NiCo/nitrogen-doped carbon (NC)-tannic acid (TA)) that integrates both electronic and architectural advantages. Unlike conventional pyrolysis of zeolitic imidazolate frameworks (ZIF) that typically yields micropore-dominated carbon matrices, the tannic acid etching strategy simultaneously creates an unclosed hollow morphology, introduces mesopores, and enhances surface hydrophilicity. This multifunctional modification significantly improves the accessibility of active sites. Density functional theory (DFT) computations revealed that monometallic Co–N_4 configuration exhibits optimized bifunctional catalytic activity over Ni–N_4 site, as evidenced by lower energy barriers for critical steps. Calculation results confirmed that Ni-mediated electronic modulation induces charge redistribution at Co–N_4 sites, while the electronic coupling effect synergistically optimizes the adsorption of key intermediates (*OOH, *O, and *H) through d-band center downshifting (ε_d = −1.2 vs. −0.54 eV in monometallic Co/NC-TA). In alkaline ORR assessments, NiCo/NC-TA exhibited superior performance compared to Pt/C-20%, achieving a half-wave potential of 0.896 V and maintaining 98% current retention after 10 h stability testing. This exceptional ORR activity and durability are attributed to the synergistic effects of the unclosed hollow morphology, mesoporous structure, and enhanced surface hydrophilicity introduced by tannic acid etching. Furthermore, NiCo/NC-TA-based Zn–air batteries demonstrated a high open-circuit voltage (1.49 V), a specific capacity (764.1 mAh·g^{-1}), and outstanding long-term cycling stability. Additionally, the catalyst exhibited competitive HER activity, with a low overpotential (92 mV) in alkaline media, matching the performance of Pt/C-20% at a current density of 120 mA·cm^{-2}.

2 Experimental

All chemicals were commercially available and had not undergone further purification. In the experimental process, $Zn(NO_3)_2{\cdot}6H_2O$ (analytical reagent (AR)) was sourced from the XiHua brand, $Co(NO_3)_2{\cdot}6H_2O$ (AR) and $Ni(NO_3)_2{\cdot}6H_2O$ (AR) were sourced from the Comie brand, tannic acid (American Chemical Society (ACS) grade) was sourced from the Aladdin brand. Ruthenium oxide and 2-methylimidazole (AR) were obtained from the Aladdin brand. Pt/C (20 wt.%) was purchased from Alfa Aesar, and Nafion solution (5 wt.%) was purchased from DuPont. Methanol and ethanol were supplied by Tianjin Fuyu Reagents.

2.1 Synthesis of surface modification precursors

0.87 g of $Zn(NO_3)_2{\cdot}6H_2O$ (2.9 mmol), 0.0145 g of $Co(NO_3)_2{\cdot}6H_2O$ (0.05 mmol), and 0.0145 g of $Ni(NO_3)_2{\cdot}6H_2O$ (0.05 mmol) were dissolved in 30 mL of methanol to obtain Solution A. 1.97 g of 2-methylimidazole (0.024 mol) was dissolved in 20 mL of methanol to obtain Solution B. Solution A was added dropwise into Solution B, and the mixture was stirred at room temperature for 24 h. The resulting methanol solution was centrifuged and then vacuum dried to obtain NiCo-ZIF. 0.1 g of the product was dissolved in 50 mL of methanol and aged in 250 mg of TA (5 g·L^{-1}) for 10 min. After aging, the methanol solution was centrifuged to obtain the sample NiCo-ZIF-TA.

2.2 Synthesis of NiCo/NC-TA catalyst

The obtained NiCo-ZIF-TA, NiCo-ZIF, Co-ZIF-TA, and Ni-ZIF-TA were placed in a tubular furnace and heated at a rate of 2 °C·min^{-1} to 920 °C under a N_2 atmosphere, calcined for 3 h, and cooled naturally to room temperature to obtain the target samples NiCo/NC-TA, NiCo/NC, Co/NC-TA, and Ni/NC-TA, respectively.

The procedure exclusively involved adding a single metal salt (either Co or Ni salt) to fabricate monometallic catalysts Co/NC-TA and Ni/NC-TA, while the NiCo/NC catalyst was synthesized without etching step.

More details of testing and characterization information can be found in the Electronic Supplementary Material (ESM).

3 Results and discussion

3.1 Structural characteristics

As illustrated in the procedure shown in Fig. 1(a), NiCo/NC-TA with a hollow architecture was fabricated through chemical etching of a ZIF precursor followed by pyrolysis. Zn/Co/Ni-containing ZIF was first prepared by mixing methanol solutions of Zn^{2+}, Co^{2+}, and Ni^{2+} salts with 2-methylimidazole, followed by tannic acid etching to selectively remove unstable metal nodes and induce defect formation. Subsequent pyrolysis yielded the final open-hollow catalyst NiCo/NC-TA. As revealed by the scanning electron

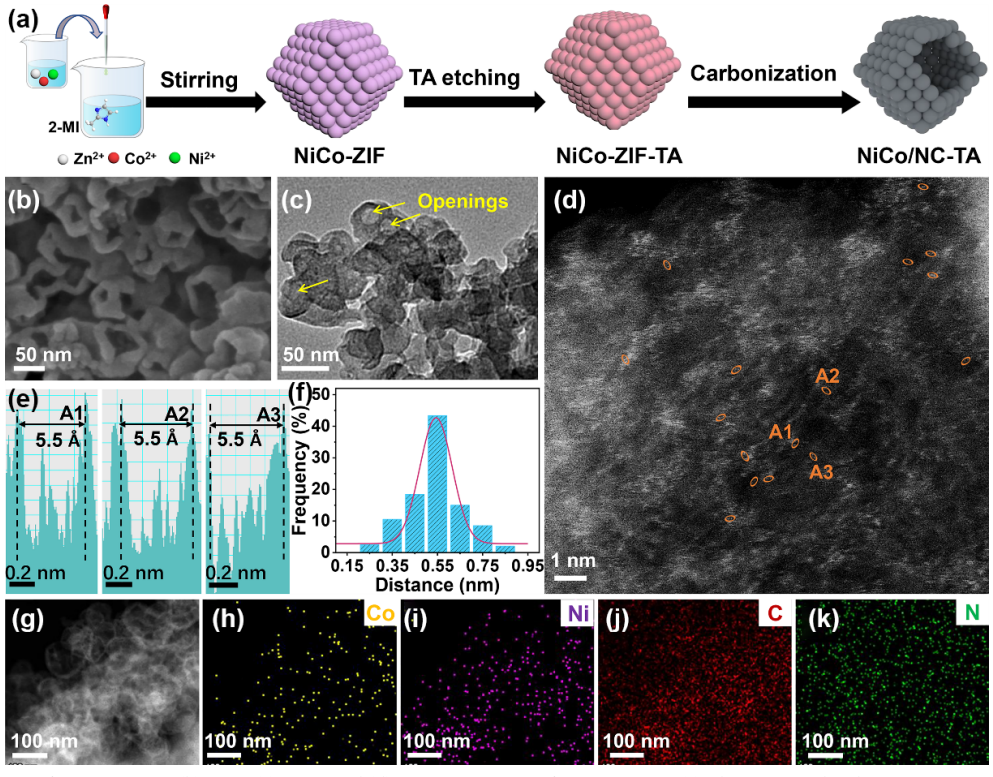

Figure 1 (a) Preparation of NiCo/NC-TA. (b) SEM, (c) TEM, and (d) AC-TEM images of NiCo/NC-TA. (e) The intensity distributions corresponding to areas A1, A2, and A3 in (d). (f) The statistical Co–Ni distance in the observed diatomic pairs. ((g)–(k)) High-angle annular dark-field scanning TEM (HAADF-STEM) image and elemental mapping images of Co, Ni, C, and N of NiCo/NC-TA.

microscopy (SEM) image, the synthesized NiCo/NC-TA exhibits a relatively uniform particle size distribution, with an average diameter of approximately 50 nm (Fig. 1(b)). Consistent with the proposed tannic acid etching strategy, the resulting carbon framework presents a distinct open aperture on the dodecahedral structure, which is crucial for enhancing active site accessibility (Figs. 1(b) and 1(c)). X-ray powder diffraction (XRD) patterns (Fig. S2 in the ESM) revealed the absence of distinct metal diffraction peaks in all samples, indicating the high dispersion of Ni/Co species. The presence of single atoms was evidenced by the appearance of paired bright spots in the imagery using spherical aberration-corrected transmission electron microscopy (AC-TEM) (Fig. 1(d)). Intensity distribution analysis from randomly selected regions confirmed the homogeneous dispersion of single atoms in the NiCo/NC-TA catalyst, with an average interatomic spacing of approximately 5.5 Å (Fig. 1(e)). We further performed statistical measurement of the interatomic distances from the aberration-corrected images of NiCo/NC-TA (Fig. S3 in the ESM). The resulting distribution (Fig. 1(f)) reveals a normal distribution with the majority of distances concentrated around 5.5 Å, providing further evidence that the interatomic spacing between Ni and Co is approximately 5.5 Å. Elemental mapping (Figs. 1(g)–1(k)) demonstrates homogeneous distribution of Co, Ni, N, and C throughout the samples.

For further investigation, the electronic properties were detected. In Fig. 2(a), all specimens exhibited G-band (1585 cm^{-1}) and D-band (1340 cm^{-1}) features, corresponding to sp^2-hybridized carbon atoms and carbon lattice defects, respectively. NiCo/NC-TA catalyst exhibited a higher defect density (intensity ratio of the D and G bands (I_D/I_G) = 1.05) compared to NiCo/NC (1.02), Co/NC-TA (1.01), and Ni/NC-TA (1.03), which can be attributed to the synergistic effects of tannic acid etching-induced lattice distortion and the Ni/Co dual-metal synergy [19, 25]. The specific surface area of the NiCo/NC-TA catalyst reaches 550 $cm^2 \cdot g^{-1}$ (Fig. 2(b)), higher than that of NiCo/NC (275 $cm^2 \cdot g^{-1}$) and Co/NC-TA (404 $cm^2 \cdot g^{-1}$), which can be attributed to the etching of tannic acid [26]. The higher surface area, compared to NiCo/NC, Ni/NC-TA, and Co/NC-TA, facilitates mass transport of reactive intermediates during electrocatalytic process. Hydrophilicity assessments via contact angle measurements (Fig. 2(c)) revealed that NiCo/NC-TA possesses enhanced wettability (26° vs. 79° of NiCo/NC), ensuring the utilization of subsurface active sites [27]. Fourier-transform infrared (FTIR) spectra analysis was conducted to identify the reasons for the improved hydrophilicity. In Fig. S4 in the ESM, in comparison with the untreated precursor NiCo-ZIF, the tannic acid-treated precursor NiCo-ZIF-TA exhibited a broad peak at 3250 cm^{-1}, which indicates the presence of free hydroxyl groups (–OH) in the structure. Additionally, a stretching vibration peak of carbonyl groups (C=O) appeared at 1700 cm^{-1}, suggesting the formation of ester bonds. At 1600 cm^{-1}, the intensity of the stretching vibration peak of C–O bonds was enhanced, demonstrating the existence of a relatively large number of C–O bonds. Furthermore, a peak corresponding to C–O–C bonds was observed at 1050 cm^{-1}, indicating the formation of C–O–C bonds. FTIR and X-ray photoelectron spectroscopy (XPS) were employed to analyze the surface oxygen functionality of the pyrolytic products prepared with (NiCo/NC-TA) and without (NiCo/NC) tannic acid etching. FTIR spectra (Fig. S5 in the ESM) indicate that both samples contain signatures of O–C=O, C–OH, and C–O–C, along with a broad O–H stretching vibration near 3500 cm^{-1} [28]. However, the O–H band is significantly stronger in NiCo/NC-TA, suggesting a higher density of surface hydroxyl groups, which aligns

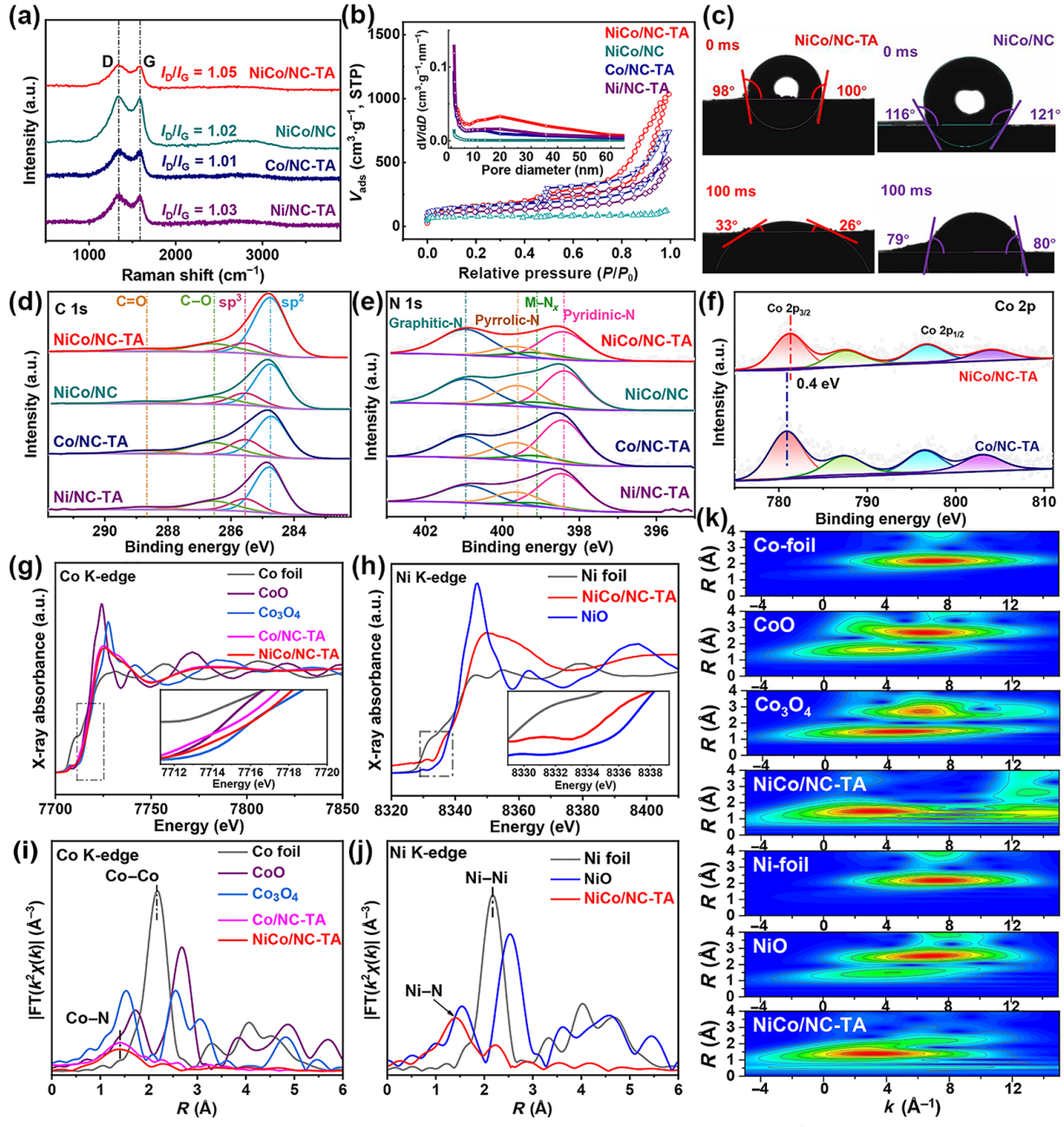

Figure 2 (a) Raman spectra and (b) nitrogen adsorption–desorption isotherms and corresponding pore size distribution for NiCo/NC-TA, NiCo/NC, Co/NC-TA, and Ni/NC-TA. (c) Contact angle results of NiCo/NC-TA and NiCo/NC. High-resolution XPS spectra of (d) C 1s, (e) N 1s, and (f) Co 2p. XANES spectra of (g) Co K-edge and (h) Ni K-edge. k^3-weighted FT-EXAFS spectra of (i) Co and (j) Ni at R space. (k) WT contour plots.

with the observed enhanced hydrophilicity (Fig. 2(c)). The result is corroborated by XPS O 1s analysis (Fig. S6 in the ESM), which shows a higher proportion of C–OH species in NiCo/NC-TA (35.4% vs. 27.6% in NiCo/NC). These results demonstrate that the tannic acid etching-pyrolysis process yields the final product rich in oxygenated groups (e.g., hydroxyl and carboxyl), which improves the surface hydrophilicity [29, 30]. To elucidate the chemical states of the elements, XPS and X-ray absorption spectroscopy (XAS, including X-ray absorption near-edge structure (XANES) and extended X-ray absorption fine structure (EXAFS)) analyses were conducted. C 1s XPS spectra of the NiCo/NC-TA, NiCo/NC, Ni/NC-TA, and Co/NC-TA catalysts were deconvoluted to reveal four peaks (Fig. 2(d)), corresponding to sp^2 carbon (284.8 eV), sp^3 carbon (285.5 eV), C–O (286.6 eV), and C=O (288.8 eV) functionalities [31]. Typically, the defect level was determined through the ratio of the two types of carbon (sp^2 carbon and sp^3 carbon atoms) [32, 33]. The sp^2/sp^3 ratio (Table S3 in the ESM) of NiCo/NC-TA (5.73) is higher than that of Ni/NC-TA (3.69), NiCo/NC (3.56), and Co/NC-TA (2.58), indicating a higher surface defect content in NiCo/NC-TA, which is consistent with the Raman spectra (Fig. 2(a)). The N 1s XPS spectra (Fig. 2(e)) revealed four distinct peaks attributed to pyridinic-N (398.4 eV), metal–N (399.8 eV), pyrrolic-N (400.7 eV), and graphitic-N (401.3 eV) [34–36]. The quantitative analysis of NiCo/NC-TA (Fig. S7 in the ESM) shows an optimal nitrogen speciation for the ORR, with high contents of metal–N, graphitic-N, and pyridinic-N serving to

provide active sites, improve conductivity, and modulate intermediate adsorption, respectively [37–39]. Compared to Co/NC-TA, the Co 2p binding energy in NiCo/NC-TA exhibited a positive shift of approximately 0.4 eV, indicating a higher oxidation state of Co due to the electron-withdrawing effect of Ni (Fig. 2(f)) [40]. The Co K-edge XANES spectra (Fig. 2(g)) revealed the valence state differences between NiCo/NC-TA and the reference samples Co/NC-TA, Co foil, CoO, and Co_3O_4. The first derivative of the Co K-edge XANES further elucidated the exact valence state of Co [41]. The absorption edge position of NiCo/NC-TA was located between CoO and Co_3O_4, indicating that the oxidation state of Co in NiCo/NC-TA is between +2 and +3, and higher than that in Co/NC-TA [42, 43]. This is likely due to the electron-withdrawing effect of Ni atoms, leading to an increased electron density around Co atoms. The Ni K-edge of the NiCo/NC-TA catalyst was positioned between Ni foil and NiO (Fig. 2(h)), suggesting that the valence state of Ni is between 0 and +2 due to charge transfer to adjacent Co sites [19, 43]. From the analysis of the Fourier transform k^3-weighted extended X-ray absorption fine structure spectrum at the Co K-edge (Fig. 2(i)) for the NiCo/NC-TA detected at 1.5 Å in *R* space, which can be attributed to Co–N coordination bonds, and no Co–Co coordination peaks are observed, confirming the presence of isolated Co atoms in the NiCo/NC-TA [44, 45]. For the Ni K-edge FT-EXAFS spectra (Fig. 2(j)), a primary peak corresponding to Ni–N coordination at 1.42 Å is observed, indicating that Ni atoms are also dispersed in a single-atom form without forming Ni nanoparticles or clusters [46]. Additionally, no Ni–Co bonds were observed, thus excluding the possibility of Ni–Co bonds in NiCo/NC-TA and the formation of Ni–Co clusters. To further substantiate the presence of Ni and Co in a single-atom form, wavelet transform (WT) analysis was employed. As shown in Fig. 2(k), the Ni–N coordination bonds in the NiCo/NC-TA catalyst are distinctly visible at a wavelet transform domain of 3.7 $Å^{-1}$, contrasting with the spectra of Ni foil and NiO. Meanwhile, the Co–N coordination bonds are prominently observed at 4.0 $Å^{-1}$, differing from the spectra of Co foil, CoO, and Co_3O_4. These results strongly support the conclusion that isolated $Ni–N_4$ and $Co–N_4$ structural units coexist in the NiCo/NC-TA catalyst.

3.2 Electrocatalysis performance

ORR performance was evaluated in 0.1 M KOH with saturated O_2. According to the plots from cyclic voltammetry (CV) and linear sweep voltammetry (LSV) measurements (Fig. S8 in the ESM and Fig. 3(a)), the NiCo/NC-TA electrocatalyst exhibited superior activity with a high half-wave potential of 0.896 V vs. reversible hydrogen electrode (RHE), which significantly outperformed Pt/C-20% (0.823 V), the single-metal catalysts Co/NC-TA (0.821 V), Ni/NC-TA (0.722 V), and the unetched NiCo/NC (0.809 V).

The calculated kinetic current densities (j_k) of NiCo/NC-TA

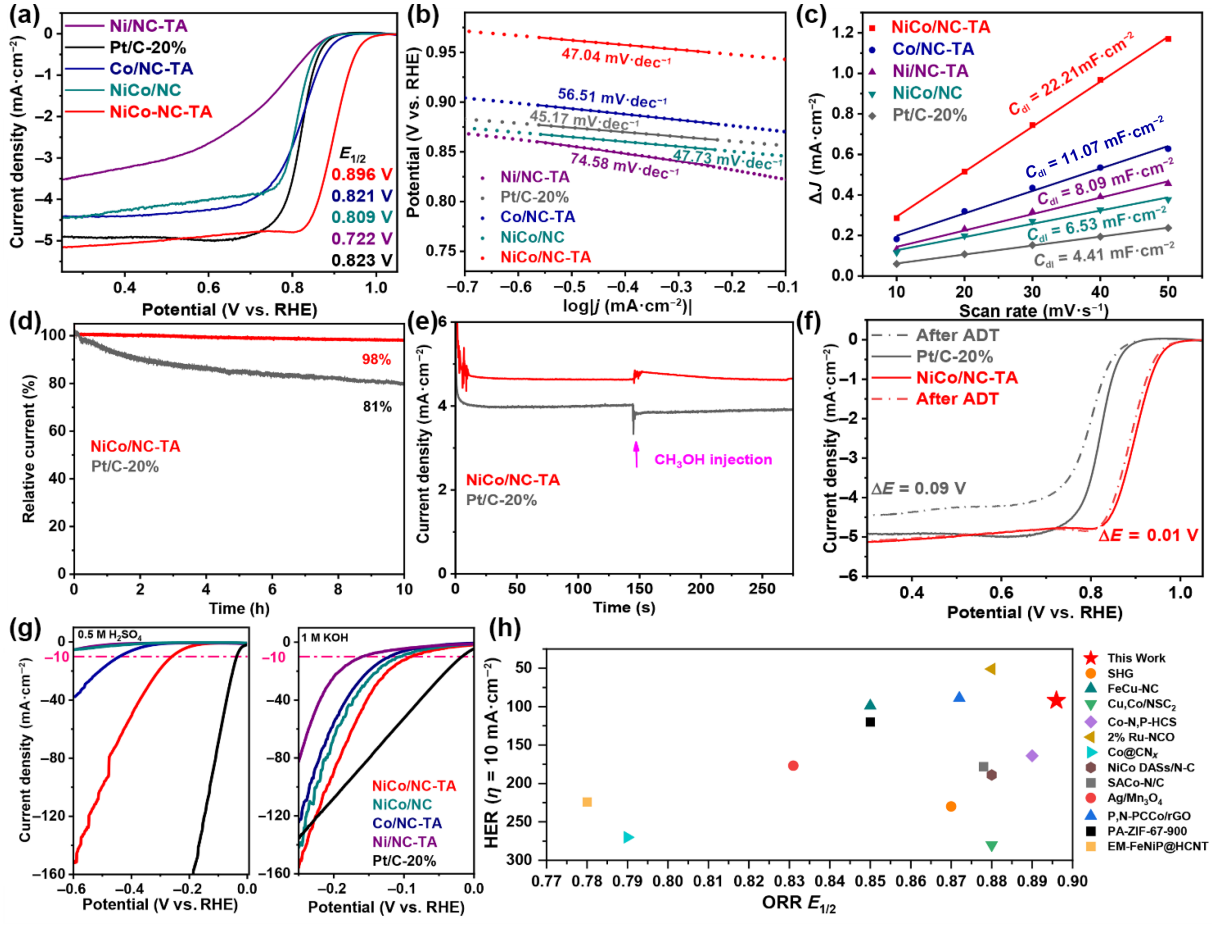

Figure 3 (a) LSV curves and (b) Tafel plots of NiCo/NC-TA, NiCo/NC, Co/NC-TA, Ni/NC-TA, and Pt/C-20% for ORR in 0.1 M KOH. (c) The variation of capacitive current density with respect to scan rates for electrocatalysts in the non-Faradaic region. (d) Chronoamperometric plots recorded at 0.6 V vs. RHE for 10 h of NiCo/NC-TA and Pt/C-20%. (e) Methanol tolerance tests of NiCo/NC-TA and Pt/C-20%. (f) LSV curves of NiCo/NC-TA and Pt/C-20% before and after ADT. (g) LSV curves for HER tests. (h) Electrocatalytic performance comparison of the published bifunctional catalysts.

reached 39.53 mA·cm^{-2} at 0.85 V (Fig. S9 in the ESM), surpassing those of the other comparative samples, confirming the superior reaction kinetics. The lowest Tafel slope of 47.04 mV·dec^{-1} for NiCo/NC-TA outperforms other catalysts, demonstrating superior reaction kinetics (Fig. 3(b)). To assess the available active surface area of obtained catalysts, the double-layer capacitance (C_{dl}) in the non-Faradaic region was determined at different scan rates (Fig. S10 in the ESM). NiCo/NC-TA exhibited a larger double-layer capacitance and the electrochemical surface area (C_{dl} = 22.21 mF·cm^{-2}, electrochemically active surface area (ECSA) = 555.25 m^2·g^{-1}), indicating the highest number of exposed active sites, which is related to the larger specific surface area and mesoporous of NiCo/NC-TA (Fig. 3(c)). The turnover frequency (TOF) value of NiCo/NC-TA (7.3 s^{-1} in 0.85 V vs. RHE) was superior to that of the other comparative samples (0.1 s^{-1} for Pt/C-20%, 0.3 s^{-1} for Co/NC-TA, 1.4 s^{-1} for Ni/NC-TA, and 0.3 s^{-1} for NiCo/NC in Table S4 in the ESM), indicating the superior intrinsic activity. To determine the electron transfer number (n) during ORR, rotating disk electrode (RDE) and rotating ring-disk electrode (RRDE) tests were conducted. The number of transferred electrons was calculated based on the Koutecký–Levich (K–L) equation (for RDE) and hydrogen peroxide yield (for RRDE), respectively. The relevant data were presented in Figs. S11 and S12 in the ESM. For the NiCo/NC-TA sample, the calculated electron transfer numbers were 3.92 and 4 (from RRDE and RDE methods, respectively), confirming the 4-electron ORR pathway. Co/NC-TA, NiCo/NC, and Pt/C-20% catalysts demonstrate the 4-electron reduction. In contrast, Ni/NC-TA shows a much lower n value (~ 2.01), consistent with a 2-electron pathway yielding H_2O_2 (Fig. S11 in the ESM). Moreover, the 2-electron catalytic performance of the Ni/NC-TA catalyst is still comparable to that of the catalysts reported in Ref. [47]. The current decay of NiCo/NC-TA was only 2% after 10 h in the stability test, while Pt/C-20% catalyst maintained only 81% (Fig. 3(d)), providing strong evidence of the reliable stability of the NiCo/NC-TA catalyst. The methanol tolerance tests for NiCo/NC-TA and Pt/C-20% was determined by adding 3 mL of methanol to the 0.1 M KOH electrolyte (Fig. 3(e)). The current density of NiCo/NC-TA only experienced slight disturbance upon the addition of methanol, more stable than Pt/C-20%. In stark contrast, NiCo/NC-TA demonstrated the high tolerance to methanol, with its electrocatalytic activity remaining largely unaffected, which could expand its application capabilities in other energy storage devices (such as fuel cells). Accelerated degradation tests (ADT) also revealed the durability of NiCo/NC-TA, with only a 10 mV decay in half-wave potential and nearly unchanged limiting current after 10,000 cycles (Fig. 3(f)).

In addition to exhibiting high performance in oxygen reduction electrochemistry, NiCo/NC-TA also demonstrated superior HER activity in 1.0 M KOH and 0.5 M H_2SO_4. In alkaline environment, the NiCo/NC-TA catalyst achieves a current density of 10 mA·cm^{-2} with an overpotential of only 92 mV, while this value is 257.7 mV in acidic environment, and both of which are significantly lower than the required overpotentials for the Ni/NC-TA (165 mV in 1 M KOH), Co/NC-TA (126 mV in 1 M KOH and 442 mV in 0.5 M H_2SO_4), and NiCo/NC (110 mV in 1 M KOH) catalysts, as evidenced in Fig. 3(g). Moreover, the obtained NiCo/NC-TA demonstrates advantageous mass activity for the HER in alkaline media, as evidenced by a direct comparison with commercial Pt/C-20% following normalization of the current density to the catalyst loading (Fig. S13 in the ESM). Additionally, the stability of NiCo/NC-TA for HER was evaluated by chronopotentiometry in 1.0 M KOH electrolyte. The current density curve for the HER remained stable throughout the 60 h test period (Fig. S14 in the ESM). Furthermore, a comparative analysis of recently reported bifunctional catalysts reveals that the obtained NiCo/NC-TA exhibits comparable multifunctional performance, as illustrated in Fig. 3(h) (Table S5 in the ESM). The OER performance under alkaline conditions was evaluated on RDE in 1.0 M KOH. As illustrated in Fig. S15 in the ESM, the NiCo/NC-TA catalyst required an overpotential of 420 mV to achieve a current density of 10 mA·cm^{-2}, which is higher than that of commercial RuO_2 under identical testing conditions. These results indicate that the catalyst exhibits certain OER activity, but its performance is insufficient to serve as a bifunctional oxygen electrocatalyst in rechargeable air electrodes due to insufficient catalytic efficiency and stability.

3.3 Density functional theory calculation

In-situ Raman spectroscopy was utilized to directly monitor the dynamic structural and electronic evolution of active sites in the NiCo/NC-TA catalyst during the ORR process, providing atomic-level insights into the underlying reaction mechanisms. Throughout the testing, the I_D/I_G ratio remained stable, confirming the high structural stability of the NiCo/NC-TA electrocatalyst during ORR test. At the initial state, no pronounced peaks were observed as shown in Fig. 4(a), indicating that the ORR had not yet commenced. Upon increasing the potential to 1.1 V vs. RHE, a new peak emerged at 605 cm^{-1}, which was attributed to the formation of CoOOH [48]. As the potential was decreased, a peak at 500 cm^{-1} gradually became apparent, indicative of the formation of $Co(OH)_2$, thus revealing the transformation from CoOOH to Co(OH) during the ORR process [19]. In addition, the peak at 1048 cm^{-1} is characteristic of the *OH mode. With the negative shift in potential, the intensity of these peaks increased, suggesting a significant interaction between the Co–N active sites in NiCo/NC-TA and the superoxide ion *OOH. These findings provide insights into the catalytic behavior of the NiCo/NC-TA electrocatalyst in the ORR process.

To further elucidate the origins of the catalytic performance in the ORR and HER of the NiCo/NC-TA catalyst, DFT simulation calculations were conducted. Based on the XAS results, Ni–N_4, Co–N_4, and Ni–N_4/Co–N_4 models were constructed and optimized, representing the Ni/NC-TA, Co/NC-TA, and NiCo/NC-TA catalysts, respectively (Fig. S16 in the ESM). The distance between Ni and Co atoms was approximately 5.5 Å, consistent with the result from Fig. 1(e). Comparison analysis of the charge density difference (Figs. 4(b) and 4(c)) revealed that the Co atoms in Co/NC-TA and NiCo/NC-TA lost 0.9128e$^-$ and 0.9638e$^-$, respectively. After introducing Ni atoms into the NiCo/NC-TA system, more charge was transferred from the Co–N_4, which is consistent with the higher oxidation state of Co (Figs. 2(f) and 2(g)). The proposed ORR reaction mechanisms for NiCo/NC-TA are summarized in Fig. 4(c). ORR Pathways 1 and 2 correspond to the ORR pathways occurring at the Co and Ni sites, respectively, involving the formation and conversion of *O_2, *OH, *OOH, and *O intermediates in Pauling model. ORR Pathway 3 depicts a mechanism where O_2 adsorbs in a bridging configuration (O–O) across paired Co–Ni sites (Co–O–O–Ni). This mechanism involves O–O bond cleavage, leading to *OH formation at the Co site and *O formation at the Ni site, followed by the subsequent formation and dissociation of *OH on both the Ni and Co sites. Analysis of

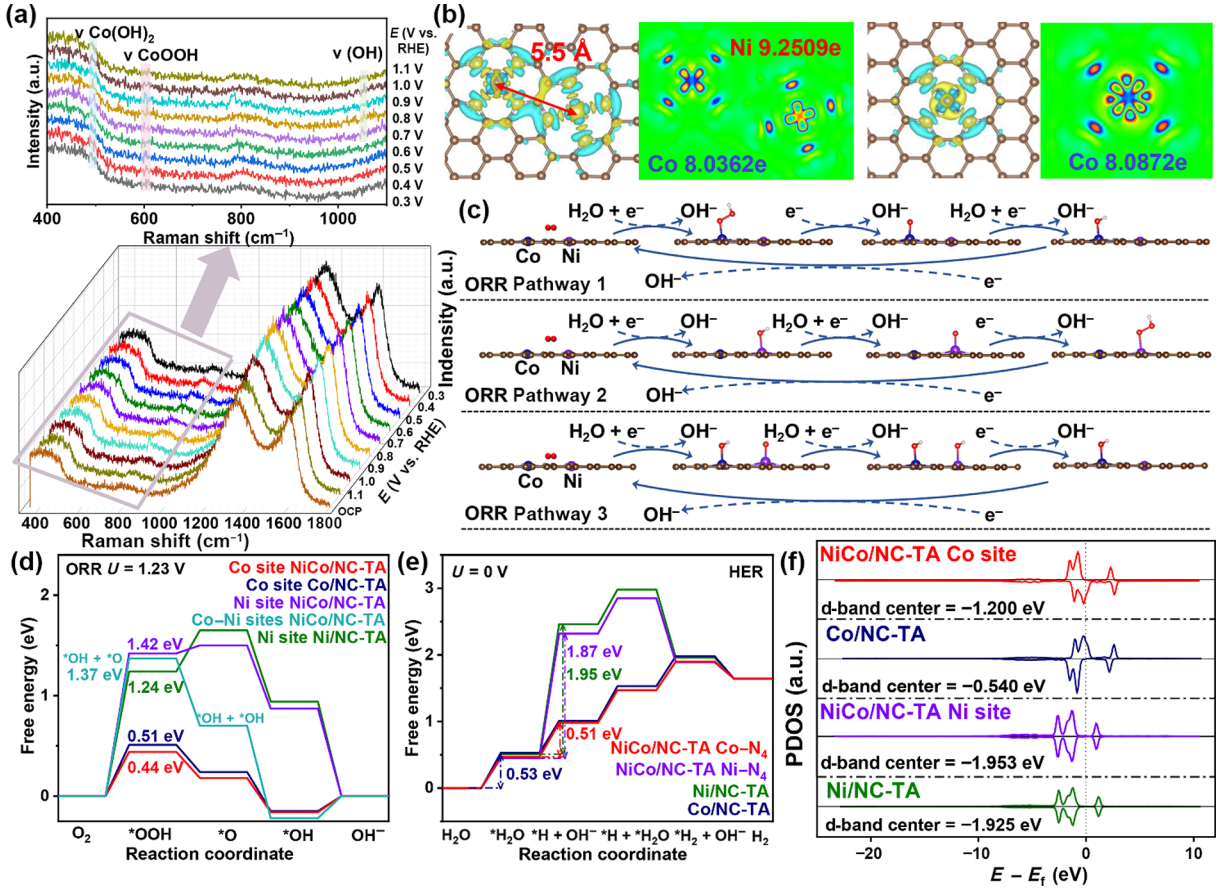

Figure 4 (a) *In-situ* Raman spectra of NiCo/NC-TA in 0.1 M KOH. (b) Charge density difference profiles of NiCo/NC-TA and Co/NC-TA (yellow represents charge accumulation and cyan represents charge depletion). (c) ORR reaction schemes for the Co site (Pathway 1), Ni site (Pathway 2), and adjacent Co and Ni sites (Pathway 3) of NiCo/NC-TA. Gibbs free energy diagrams of (d) ORR at 1.23 V and (e) HER at 0 V. (f) The PDOS plot.

these mechanisms identifies the *OH + *O formation step in the dual-site pathway as the rate-determining step (RDS), with a calculated barrier of 1.37 eV (Fig. 4(d)), implying high overpotential and low feasibility. Gibbs free energy profiles in Fig. 4(d) reveal that the mechanisms on single sites possess lower energy barriers compared to the dual-site pathway. Notably, the Co–N_4 site in NiCo/NC-TA exhibits the lowest energy barrier among all configurations for the ORR. Furthermore, the Ni–N_4 sites in Ni/NC-TA and NiCo/NC-TA have higher energy barrier for the *OOH → *O step, thus tending to the protonation process, with improved 2e^- selectivity. Compared to Ni–N_4, the Co–N_4 sites are more prone to O–O bond cleavage, favoring a 4e^- pathway. This result indicates that Co–N_4 site is the active site on the NiCo/NC-TA, while the Ni–N_4 site serves as a modulator. The DFT-calculated mechanisms for HER under acidic and alkaline conditions are elucidated. For acidic HER, the Volmer step (*H formation) is rate-determining. Comparative energy barriers (Fig. S17 in the ESM) show the Co site in the NiCo model possesses the lowest barrier (0.16 eV), substantially lower than the Ni site (1.5 eV) and the isolated Co site (0.18 eV), highlighting a synergistic effect of Ni introduction. Given the significant difference in the local pH microenvironment, mechanistic model for the alkaline HER was therefore incorporated to include the water dissociation step. The HER pathway in alkaline follows the Volmer–Heyrovsky mechanism (Fig. 4(e)). While water adsorption is the RDS on a single Co site (Gibbs free energy change for hydrogen adsorption (ΔG_{*H}) = 0.53 eV), the presence of a neighboring Ni atom lowers the adsorption barrier and shifts the RDS to water dissociation (*H_2O + e^- → *H + OH^-) on the Co site, with a reduced barrier of 0.51 eV. Ni sites, however, show much higher water dissociation barriers (1.95 eV for isolated Ni site, 1.87 eV for Ni site in NiCo/NC-TA). The low calculated ΔG_{*H} on NiCo/NC-TA indicates favorable HER thermodynamics, consistent with its experimentally observed low overpotentials in both acidic and alkaline media (Fig. 3(g)). The discrepancy exists between these calculated values and the measured overpotential, which arises because the actual overpotential incorporates kinetic barriers and the energies of transient transition states, factors beyond the scope of a calculated equilibrium thermodynamic model [49]. The comparison between experimental and theoretical calculation results implies that Co is the active center of NiCo/NC-TA in ORR and HER. Furthermore, the projected density of states (PDOS, Fig. 4(f)) calculations indicate that the d-band centers of Ni and Co in NiCo/NC-TA are farther from the Fermi level compared to Ni/NC-TA and Co/NC-TA, which weakens the chemical bonds between the active sites and oxygen-containing intermediates, leading to lowering the free energy barrier for the reaction and prompting corresponding ORR and HER activity [50].

3.4 Zinc–air battery (ZAB) performance testing

Inspired by the ORR performance of the NiCo/NC-TA catalyst, ZABs were assembled using it as the cathode (see details in supporting information). The resulting battery delivered a high peak power density of 164.8 mW·cm^{-2} (Fig. 5(a)) and a high open-circuit potential of 1.49 V (Fig. 5(b)), outperforming the

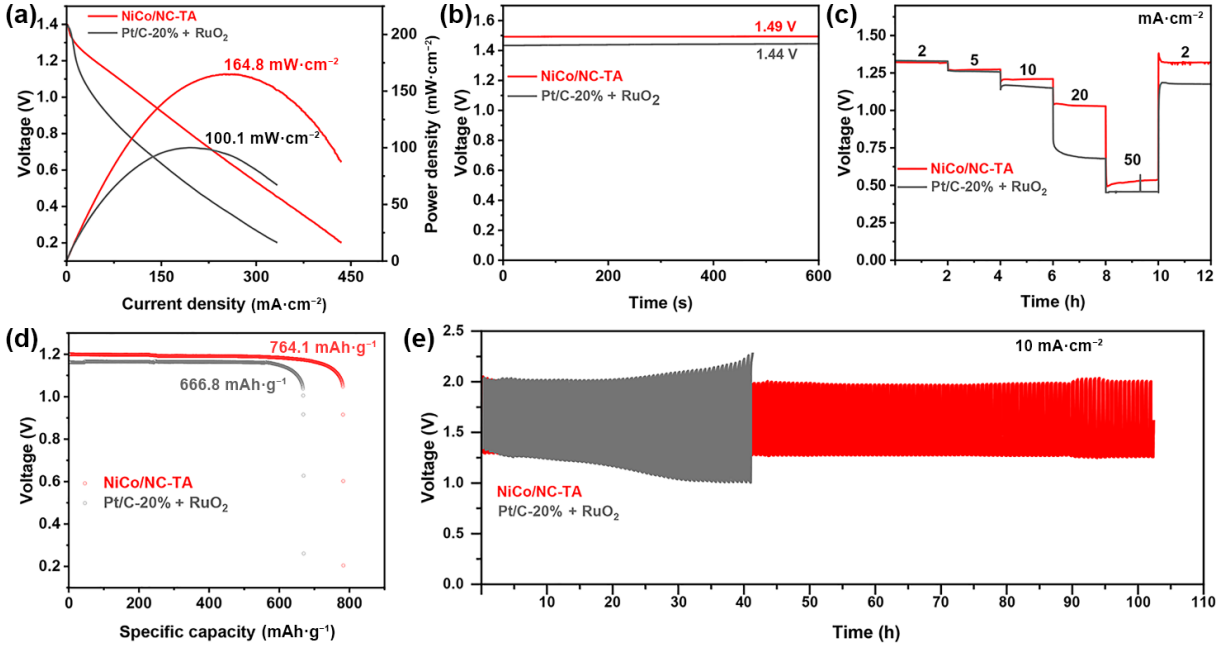

Figure 5 Performance of aqueous Zn–air batteries. (a) Discharge polarization curves and the corresponding power density curves. (b) Open-circuit voltage plot. (c) The galvanostatic discharge curves. (d) Specific capacity plots. (e) Charge–discharge cycling tests at 10 mA·cm^{-2}.

commercial Pt/C-20% + RuO_2 counterpart (100.1 mW·cm^{-2}, 1.44 V). The rate capabilities were evaluated at various current densities ranging from 2 to 50 mA·cm^{-2} (Fig. 5(c)). Notably, the capacity recovered well when the current density was returned to 2 mA·cm^{-2}, and no significant voltage drop was observed even at a high current density of 50 mA·cm^{-2}. As shown in Fig. 5(d), the NiCo/NC-TA-based ZAB also exhibited a high specific capacity of 764.1 mAh·g^{-1} at 10 mA·cm^{-2}, which is substantially higher than that of the Pt/C-20% + RuO_2-based battery (666.8 mAh·g^{-1}). Furthermore, the cycling stability of the ZABs was investigated through galvanostatic discharge–charge cycling (Fig. 5(e)). NiCo/NC-TA-based ZAB demonstrated stable cycling performance for 104 h, whereas the discharge voltage of Pt/C-20% + RuO_2-based battery dropped significantly within 42 h under identical test conditions. This result confirms the exceptional stability of NiCo/NC-TA in practical ZAB applications.

4 Conclusions

In summary, the hydrophilic open-hollow porous NiCo/NC-TA bimetallic catalyst was successfully synthesized via an etching-pyrolysis strategy. Controlled chemical etching step endows the carbon matrix with more accessible active sites. Benefiting from the high specific surface area, abundant mesopores, defect-rich structure, hydrophilic surface, and optimized electronic configuration, NiCo/NC-TA exhibited high-performance toward ORR and HER. Experimental and DFT calculation results demonstrated that Co is the active center of NiCo/NC-TA in ORR and HER. The introduction of Ni facilitates electron outflow from Co sites with a downshifted d-band center, which effectively mitigates intermediate over-adsorption and reduces energy barriers for multiple rate-determining steps, thereby enhancing ORR and HER performances. Compared to commercial Pt/C-20%, NiCo/NC-TA also exhibited promising application potential in ZAB evaluations, showing competitive electrochemical performance in key metrics, such as power density, specific capacity, and long-term stability. This work offers a new approach for efficient metal–N–C catalysts in energy storage and conversion.

Electronic Supplementary Material: Supplementary material (details of characterizations, electrochemical measurements, and density function theory, SEM images of NiCo/NC, Co/NC-TA, and Ni/NC-TA, XRD patterns, inductively coupled plasma (ICP) results, Brunauer–Emmett–Teller (BET) surface area and pore volume, FTIR spectra, O 1s, C 1s, and N 1s XPS spectra, further details of electrochemical test, catalyst structure simulation diagrams, Gibbs free energy diagrams of HER at 0 V in an acidic environment) is available in the online version of this article at https://doi.org/10.26599/NR.2026.94908401.

Data availability

All data needed to support the conclusions in the paper are presented in the manuscript and the Electronic Supplementary Material. Additional data related to this paper may be requested from the corresponding author upon request.

Acknowledgements

This work was supported by the National Natural Science Foundation of China (No. 22402185), the Natural Science Foundation of Henan Province (Nos. 242300421633 and 242102230007), Science and Technology Project of Henan Province (No. 262102231076), Doctoral Research Fund and Youth Cultivation Fund of Zhengzhou University of Light Industry (Nos. 2023BSJJ009 and 2024XNQNPY25), and Henan International Science and Technology Cooperation Key Project (No. 252102520051).

Declaration of competing interest

All the contributing authors report no conflict of interests in this work.

Author contribution statement

X. X. L.: Writing – original draft, Writing – review & editing, conceptualization, data curation, methodology, validation, project administration, funding acquisition. Y. H. W.: Writing – original draft, visualization, data curation, validation, investigation, formal analysis. F. S. T.: Data curation, validation, visualization. P. L. L.: Data curation, validation. Z. Y. F.: Data curation, validation. G. Q. W.: Project administration, resources. H. Y.: Resources, methodology. H. W.: Funding acquisition, resources, supervision. J. B. Z.: Project administration, funding acquisition, writing – review & editing, supervision. All the authors have approved the final manuscript.

Use of AI statement

None.

References

[1] Chen, G. B.; Lu, R. H.; Li, C. Z.; Yu, J. M.; Li, X. D.; Ni, L. M.; Zhang, Q.; Zhu, G. Q.; Liu, S. W.; Zhang, J. X. et al. Hierarchically porous carbons with highly curved surfaces for hosting single metal FeN_4 sites as outstanding oxygen reduction catalysts. *Adv. Mater.* **2023**, *35*, 2300907.

[2] Son, Y. J.; Mirshekari, G.; Raaijman, S. J.; Corbett, P. J. Technology landscape of anion exchange membrane water electrolyzers: Where are we today? *ACS Energy Lett.* **2025**, *10*, 3058–3063.

[3] Lv, Z. P.; Zhang, H. K.; Liu, C. H.; Li, S. L.; Song, J. X.; He, J. L. Oxygen-bridged cobalt-chromium atomic pair in MOF-derived cobalt phosphide networks as efficient active sites enabling synergistic electrocatalytic water splitting in alkaline media. *Adv. Sci.* **2024**, *11*, 2306678.

[4] Alemayehu, D. D.; Tsai, M. C.; Tsai, M. H.; Yang, C. C.; Chang, C. C.; Chang, C. Y.; Moges, E. A.; Lakshmanan, K.; Nikodimos, Y.; Su, W. N. et al. Heterogeneous interfaces of Ni_3Se_4 nanoclusters decorated on a Ni_3N surface enhance efficient and durable hydrogen evolution reactions in alkaline electrolyte. *J. Am. Chem. Soc.* **2025**, *147*, 16047–16059.

[5] Wang, D.; Li, X. S.; Ren, P. H.; Wei, Y. K.; Li, R. P.; Chen, Y. K.; Wang, W. C.; Yang, P. X.; Chen, Z. D. Asymmetric N, P-coordinated Co single atom catalyst for efficient oxygen reduction reaction in Zn–air batteries. *Appl. Catal. B: Environ. Energy* **2025**, *375*, 125436.

[6] Yang, X. H.; Mao, H. N.; Zhou, Z. N.; Li, K. R.; Li, C.; Ye, Q.; Liu, B. P.; Fang, Y. P.; Cai, X. Biphasic nanoalloys-based trifunctional monolith for high-performance flexible Zn–air batteries and self-driven water splitting. *Adv. Funct. Mater.* **2024**, *34*, 2402933.

[7] Tang, B.; Ji, Q. Q.; Zhang, X. L.; Shi, R. C.; Ma, J.; Zhuang, Z. C.; Sun, M.; Wang, H. J.; Liu, R. Q.; Liu, H. J. et al. Symmetry breaking of FeN_4 moiety via edge defects for acidic oxygen reduction reaction. *Angew. Chem., Int. Ed.* **2025**, *64*, e202424135.

[8] Chen, Y. X.; Meng, Z. H.; Wei, X. L.; Wu, M. J.; Xiong, Y. F.; Tang, H. B.; Wang, R.; Tian, T.; Wang, D. S.; Tang, H. L. Tellurium–nitrogen–carbon support boosting platinum catalysis in high-efficiency proton exchange membrane fuel cells. *Angew. Chem., Int. Ed.* **2025**, *64*, e202512315.

[9] Zhang, J.; Qu, S. Y.; Li, B.; Li, X. Y.; Lin, L. Nitrogen coordination modulation of single-atom CoN_4 enables dual-active-sites catalyst featuring synergistic organics adsorption and peroxymonosulfate activation. *Chem. Eng. J.* **2023**, *468*, 143593.

[10] He, Y. H.; Hwang, S.; Cullen, D. A.; Uddin, M. A.; Langhorst, L.; Li, B. Y.; Karakalos, S.; Kropf, A. J.; Wegener, E. C.; Sokolowski, J. et al. Highly active atomically dispersed CoN_4 fuel cell cathode catalysts derived from surfactant-assisted MOFs: Carbon-shell confinement strategy. *Energy Environ. Sci.* **2019**, *12*, 250–260.

[11] Yang, A. Z.; Su, K. Y.; Lei, W.; Tang, Y. W.; Qiu, X. Y. Ternary synergism of heterogeneous M^1N_4–C-M^2N_4–C-M^3N_4 single-atom sites to manipulate the electrocatalytic pathway for Zn–air battery and water splitting. *Adv. Energy Mater.* **2023**, *13*, 2203150.

[12] Wang, H. N.; Niu, X. X.; Liu, W. X.; Yin, R. L.; Dai, J. L.; Guo, W.; Kong, C.; Ma, L.; Ding, X.; Wu, F. F. et al. S-block metal Mg-mediated Co–N–C as efficient oxygen electrocatalyst for durable and temperature-adapted Zn–air batteries. *Adv. Sci.* **2024**, *11*, 2403865.

[13] Lv, H.; Gao, Y. F.; Li, D. S.; Yu, A. M.; Sun, C. H.; Zhang, C. M. Mediation of oxidation and spin states of Fe/P–CoO_2 core–shell structures catalysts for oxygen evolution reaction. *Adv. Funct. Mater.* **2025**, *35*, 2418334.

[14] Huang, J. Z.; Clark, A. H.; Hales, N.; Crossley, K.; Guehl, J.; Skoupy, R.; Schmidt, T. J.; Fabbri, E. Oxidation of interfacial cobalt controls the pH dependence of the oxygen evolution reaction. *Nat. Chem.* **2025**, *17*, 856–864.

[15] Fan, H. Y.; Liu, Y. R.; Li, J. X.; Lv, Z. H.; Wang, C. L.; Liu, R.; Dong, F. L.; Tian, C. G.; Feng, X.; Yang, W. X. et al. Optimizing the mass transport and atomic Fe intrinsic activity to achieve high-performing fuel cells. *J. Am. Chem. Soc.* **2025**, *147*, 18953–18962.

[16] Kundu, A.; Bolar, S.; Das, S.; Kolya, H.; Kang, C. W.; Kuila, T.; Murmu, N. C. General approach to synthesize multilayer graphitic carbon-nanotube-encapsulated NiCo alloys as trifunctional the role of. *ACS Appl. Energy Mater.* **2022**, *5*, 14445–14454.

[17] Zhang, J. Y.; Bai, X. W.; Wang, T. T.; Xiao, W.; Xi, P. X.; Wang, J. L.; Gao, D. Q.; Wang, J. Bimetallic nickel cobalt sulfide as efficient electrocatalyst for Zn–air battery and water splitting. *Nano Micro Lett.* **2019**, *11*, 2.

[18] Fu, Y.; Yu, H. Y.; Jiang, C.; Zhang, T. H.; Zhan, R.; Li, X. W.; Li, J. F.; Tian, J. H.; Yang, R. Z. NiCo alloy nanoparticles decorated on N-doped carbon nanofibers as highly active and durable oxygen electrocatalyst. *Adv. Funct. Mater.* **2018**, *28*, 1705094.

[19] Li, M.; Zhu, H. Y.; Yuan, Q.; Li, T. Y.; Wang, M. M.; Zhang, P.; Zhao, Y. L.; Qin, D. L.; Guo, W. Y.; Liu, B. et al. Proximity electronic effect of Ni/Co diatomic sites for synergistic promotion of electrocatalytic oxygen reduction and hydrogen evolution. *Adv. Funct. Mater.* **2023**, *33*, 2210867.

[20] Qin, H. Y.; Lin, G. L.; Zhang, J. Y.; Cao, X. J.; Xia, W.; Yang, H. C.; Yuan, K. N.; Jin, T.; Wang, Q. L.; Jiao, L. F. Enhanced cooperative generalized compressive strain and electronic structure engineering in W-NiN for efficient hydrazine oxidation facilitating H_2 production. *Adv. Mater.* **2025**, *37*, 2417593.

[21] Liu, H. T.; Guan, J. Y.; Yang, S. X.; Yu, Y. H.; Shao, R.; Zhang, Z. P.; Dou, M. L.; Wang, F.; Xu, Q. Metal–organic framework-derived Co_2P nanoparticle/multi-doped porous carbon as a trifunctional electrocatalyst. *Adv. Mater.* **2020**, *32*, 2003649.

[22] Liu, W. C.; Zhang, H. H.; Ye, W. B.; Xiao, B. S.; Sun, Z. F.; Cheng, Y.; Wang, M. S. Regulating the wettability of hard carbon through open mesochannels for enhanced K^+ storage. *Small* **2023**, *19*, 2300605.

[23] Hui, Y.; Wang, L.; Xiao, F. S. Catalysis enhanced by catalyst wettability. *ACS Nano* **2025**, *19*, 7617–7633.

[24] Zhao, X.; Wang, Y. S.; Wen, J.; Cao, L. J.; Wang, F. L.; Lei, K. S.; Fang, R. Q.; Zhou, L. N.; Li, Y. W. High-curvature interfaces induce nondegenerate splitting of d-orbital energy levels for enhanced catalytic activity. *J. Am. Chem. Soc.* **2025**, *147*, 19166–19177.

[25] Zhang, Y. L.; Yan, B.; Ji, C. C.; Wei, T. T.; Niu, W. B.; Lin, H.; Shi, Y. L. Heteronuclear FeN_3–CuN_3 atom pairs coordination engineering of single atom catalysts for water splitting and Zn–air batteries. *Chem. Eng. J.* **2024**, *500*, 157182.

[26] Tian, H.; Song, A. L.; Zhang, P.; Sun, K. A.; Wang, J. J.; Sun, B.; Fan, Q. H.; Shao, G. J.; Chen, C.; Liu, H. et al. High durability of Fe–N–C single atom catalysts with carbon vacancies toward the oxygen reduction reaction in alkaline media. *Adv. Mater.* **2023**, *35*, 2210714.

[27] Yao, W.; Hu, A. Q.; Ding, J. T.; Wang, N. S.; Qin, Z.; Yang, X. F.;

Shen, K.; Chen, L. Y.; Li, Y. W. Hierarchically ordered macro-mesoporous electrocatalyst with hydrophilic surface for efficient oxygen reduction reaction. *Adv. Mater.* **2023**, *35*, 2301894.

[28] Zhang, Z. X.; Tan, B. Q.; Xie, L.; Han, Z. M.; Quan, H. Y.; Chen, D. Z. Electrochemically tailoring oxygen functionalities and pores in ordered mesoporous carbon for enhanced H_2O_2 production. *Appl. Catal. B: Environ. Energy* **2025**, *379*, 125703.

[29] Cui, J. Y.; Wu, Q. L.; Li, F. F.; Yang, J.; Yin, H. L.; Zhang, H. Y.; Xiang, Y. Y.; Zhang, X.; Fu, T. M.; Li, B. et al. Selective separation of structurally similar alkaloids by graphene oxide membranes. *Sep. Purif. Technol.* **2024**, *347*, 127474.

[30] Fu, B.; Zhang, J. F.; Robinson, N.; Zhang, Z.; Zhu, Z. J.; Dong, M. Y.; Zhang, X. Y.; Kang, J.; Michalski, P.; Zhao, Z. Y. et al. Solar-driven atmospheric water production through hierarchically ordered porous carbon for self-sustaining green hydrogen production. *Adv. Mater.* **2025**, *37*, e11336.

[31] Zhang, J.; Zhao, Y. F.; Zhao, W. T.; Wang, J.; Hu, Y. F.; Huang, C. Y.; Zou, X. L.; Liu, Y.; Zhang, D. S.; Lu, X. G. et al. Improving electrocatalytic oxygen evolution through local field distortion in Mg/Fe dual-site catalysts. *Angew. Chem., Int. Ed.* **2023**, *62*, e202314303.

[32] Lu, Z. Y.; Wang, B. F.; Hu, Y. F.; Liu, W.; Zhao, Y. F.; Yang, R. O.; Li, Z. P.; Luo, J.; Chi, B.; Jiang, Z. et al. An isolated zinc–cobalt atomic pair for highly active and durable oxygen reduction. *Angew. Chem., Int. Ed.* **2019**, *58*, 2622–2626.

[33] Li, Y. Z.; Wei, B.; Zhu, M. H.; Chen, J. C.; Jiang, Q. K.; Yang, B.; Hou, Y.; Lei, L. C.; Li, Z. J.; Zhang, R. F. et al. Synergistic effect of atomically dispersed Ni–Zn pair sites for enhanced CO_2 electroreduction. *Adv. Mater.* **2021**, *33*, 2102212.

[34] Gao, S.; Yang, H.; Rao, D. W.; Wang, N.; Li, Y.; Li, J. H.; Rao, S. S.; Maouche, C.; Wu, Z. R.; Li, B. et al. Supercritical CO_2 assisted synthesis of highly accessible iron single atoms and clusters on nitrogen-doped carbon as efficient oxygen reduction electrocatalysts. *Chem. Eng. J.* **2022**, *433*, 134460.

[35] Wang, X. T.; Ouyang, T.; Wang, L.; Zhong, J. H.; Liu, Z. Q. Surface reorganization on electrochemically-induced Zn–Ni–Co spinel oxides for enhanced oxygen electrocatalysis. *Angew. Chem., Int. Ed.* **2020**, *59*, 6492–6499.

[36] Zhang, H. B.; Liu, Y. Y.; Chen, T.; Zhang, J. T.; Zhang, J.; Lou, X. W. Unveiling the activity origin of electrocatalytic oxygen evolution over isolated Ni atoms supported on a N-doped carbon matrix. *Adv. Mater.* **2019**, *31*, 1904548.

[37] Zhou, G. D.; Yan, X. L.; Zhang, T. Y.; Wang, K.; Zhang, J. T.; Guo, J. J. MOFs-derived hierarchical porous carbon supported Co@NC nanocapsules for pH universal oxygen reduction reaction and Zn–air batteries. *Appl. Surf. Sci.* **2023**, *621*, 156906.

[38] Chen, Z.; Liu, J. K.; Li, J. P.; Zhang, Y. T.; Yang, J.; Li, J.; Wang, Z. Y.; Liu, Z. Y.; Zang, S. Q. Modulating spin state of Ni single atomic center for high-performance electrocatalytic carbon dioxide reduction. *Angew. Chem., Int. Ed.* **2025**, *64*, e202506845.

[39] Feng, X.; Wu, F.; Li, Y.; Fu, Y. K.; Li, Y.; Liu, M. Q.; Gong, Y. T.; Ren, H. X.; Wu, C.; Bai, Y. Critical role of ultra-microporous tunnel structure within hard carbon in boosting sodium-ion storage. *Adv. Mater.* **2025**, *38*, e01779.

[40] Han, A. L.; Wang, X. J.; Tang, K.; Zhang, Z. D.; Ye, C. L.; Kong, K. J.; Hu, H. B.; Zheng, L. R.; Jiang, P.; Zhao, C. X. et al. An adjacent atomic platinum site enables single-atom iron with high oxygen reduction reaction performance. *Angew. Chem., Int. Ed.* **2021**, *60*, 19262–19271.

[41] Bai, Y. R.; Wang, Y. J.; Yang, Y. B.; Sun, C.; Wang, H. T.; Lee, C. F.; Li, C. Y.; Zheng, T. T.; Jiang, K. P.; Han, L. L. Unveiling the role of heteroatom doping and strain in core–shell catalysts for CO_2RR. *Chem. Eng. J.* **2025**, *507*, 160155.

[42] Pan, Y.; Wang, M. M.; Li, M.; Sun, G. X.; Chen, Y. J.; Liu, Y. Q.; Zhu, W.; Wang, B. *In-situ* construction of N-doped carbon nanosnakes encapsulated FeCoSe nanoparticles as efficient bifunctional electrocatalyst for overall water splitting. *J. Energy Chem.* **2022**, *68*, 699–708.

[43] Pei, Z. H.; Lu, X. F.; Zhang, H. B.; Li, Y. X.; Luan, D. Y.; Lou, X. W. Highly efficient electrocatalytic oxygen evolution over atomically dispersed synergistic Ni/Co dual sites. *Angew. Chem., Int. Ed.* **2022**, *61*, e202207537.

[44] Zheng, X. B.; Yang, J. R.; Li, P.; Jiang, Z. L.; Zhu, P.; Wang, Q. S.; Wu, J. B.; Zhang, E. H.; Sun, W. P.; Dou, S. X. et al. Dual-atom support boosts nickel-catalyzed urea electrooxidation. *Angew. Chem., Int. Ed.* **2023**, *62*, e202217449.

[45] Pan, Y.; Chen, Y. J.; Wu, K. L.; Chen, Z.; Liu, S. J.; Cao, X.; Cheong, W. C.; Meng, T.; Luo, J.; Zheng, L. R. et al. Regulating the coordination structure of single-atom Fe–N_xC_y catalytic sites for benzene oxidation. *Nat. Commun.* **2019**, *10*, 4290.

[46] Zeng, R. J.; Li, Y. L.; Wan, Q.; Lin, Z.; Gao, Q.; Qiu, M. H.; Dong, Z. Q.; Xiao, L. M.; Sun, C. L.; Leng, M. Y. et al. Orbital coupling of dual-atom sites boosts electrocatalytic NO oxidation and dynamic intracellular response. *Adv. Mater.* **2025**, *37*, 2416371.

[47] Wang, Y. L.; Shi, R.; Shang, L.; Waterhouse, G. I. N.; Zhao, J. Q.; Zhang, Q. H.; Gu, L.; Zhang, T. R. High-efficiency oxygen reduction to hydrogen peroxide catalyzed by nickel single atom catalysts with tetradentate N_2O_2 coordination in a three-phase flow cell. *Angew. Chem., Int. Ed.* **2020**, *59*, 13057–13062.

[48] Jiang, M.; Wang, F.; Yang, F.; He, H.; Yang, J.; Zhang, W.; Luo, J. Y.; Zhang, J.; Fu, C. P. Rationalization on high-loading iron and cobalt dual metal single atoms and mechanistic insight into the oxygen reduction reaction. *Nano Energy* **2022**, *93*, 106793.

[49] Sun, F.; Tang, Q.; Jiang, D. E. Theoretical advances in understanding and designing the active sites for hydrogen evolution reaction. *ACS Catal.* **2022**, *12*, 8404–8433.

[50] Zhang, L. J.; Jang, H.; Liu, H. H.; Kim, M. G.; Yang, D. J.; Liu, S. G.; Liu, X. E.; Cho, J. Sodium-decorated amorphous/crystalline RuO_2 with rich oxygen vacancies: A robust pH-universal oxygen evolution electrocatalyst. *Angew. Chem., Int. Ed.* **2021**, *60*, 18821–18829.